Supporting Information: Aerosol-Induced Closure of Marine Cloud Cells: Enhanced Effects in the Presence of Precipitation

Matthew W. Christensen[1], Peng Wu[1], Adam Varble[1], Heng Xiao[1], and Jerome Fast[1]

[1]Atmospheric Science & Global Change Division, Pacific Northwest National Laboratory, Richland, WA 99354, Washington, USA

Correspondence: Matthew Christensen (matt.christensen@pnnl.gov)

1 Contents of this file:

- Text S1 – S2
- Figure S1 – S12

2 Text S1

The European Centre for Medium-Range Weather Forecasts (ECMWF) ERA-5 product which provides spatially gridded meteorological profiles at 0.25-degree spatial resolution with 37 vertical pressure levels is provided once every hour (Hersbach et al., 2020). To test the sensitivity to boundary conditions, we have run WRF simulations comparing ERA5 to MERRA-2 boundary conditions. Figure S1 shows similar cloud water mixing ratios as well as its enhancement by increased aerosol concentration for both MERRA-2 and ERA5 at 13:00 UTC. The temperature profiles from WRF are also similar between reanalysis products. On average, the simulated cloud water mixing ratio values are larger when using MERRA-2 reanalysis, but the WRF simulations that use MERRA-2 also have a deeper PBL which allow for slightly higher clouds. Cloud property differences between the WRF simulations that use different reanalysis products are generally small relative to the differences between the aerosol experiments using the same meteorology. Therefore, the choice of using MERRA-2 or ERA5 reanalysis product at these scales does not significantly change the results.

3 Text S2

The derivation of the aerosol indirect radiative effect follows from the methodology described in Quaas et al. (2008b) and Christensen et al. (2023). The derivation follows from the change in reflected solar radiation caused by a change in the planetary albedo and N_d and can be written as

$$RE_{aci} = \overline{F^{\downarrow}} \frac{d\alpha}{dN_d} \overline{\Delta N_d} \tag{1}$$

where, $\overline{F^{\downarrow}}$ is the mean top of atmosphere (TOA) incoming solar radiation, α is the planetary albedo, and N_d is the droplet concentration. α can be expanded into contributions from the surface and clouds following

$$\alpha = (1 - f_c)\alpha_{clr}\phi_{atm} + \alpha_c \phi_{atm} f_c \tag{2}$$

where ϕ_{atm} is the transfer function that accounts for the average albedo of the non-cloudy air above the surface and takes an average value of 0.7 (Diamond et al., 2020). α_c can be estimated using the two-stream delta Eddington approximation as $\alpha_c = \frac{(1-g)\tau_c}{2+(1-g)\tau_c}$ where, g is the asymmetry parameter and takes a value of 0.85 for liquid clouds and τ_c is the cloud optical thickness. τ_c is approximated using an adiabatic assumption as $\tau_c = \gamma' L^{\frac{5}{6}} N_d^{\frac{1}{3}}$ where $\gamma' \approx 0.185\ \mathrm{kg}^{-5/6}\mathrm{m}^{8/3}$ and L is the LWP which is approximated as $L = (2/3)\rho_w r_e \tau_c$ (Stephens, 1978) with the density of water, ρ_w, cloud droplet effective radius, r_e, and the cloud droplet concentration, N_d.

We use the equivalent form of $N_d = \gamma\sqrt{\tau_c} r_e^{-2.5}$, where $\gamma = 1.37 \times 10^{-5}\mathrm{m}^{-0.5}$ to compute cloud droplet number concentration from cloud effective radius and optical depth variables following Grosvenor et al. (2018). Following similar approaches to (Quaas et al., 2008a) and (Christensen et al., 2022), taking the derivative of α with respect to N_d gives

$$\frac{d\alpha}{dN_d} = \phi_{atm}\left(-\alpha_{clr}\frac{\partial f_c}{\partial N_d} + \alpha_c \frac{\partial f_c}{\partial N_d} + f_c \frac{\partial \alpha_c}{\partial N_d}\right) \tag{3}$$

where cloud-free conditions give $\frac{\partial \alpha_{clr}}{\partial N_d} = 0$. The chain rule expansion of $\frac{d\alpha_c}{dN_d} = \frac{\partial \tau_c}{\partial N_d}\frac{\partial \alpha_c}{\partial \tau_c}$ can be solved by the following two derivatives: 1) $\frac{\partial \tau_c}{\partial N_d} = \frac{\tau_c}{3N_d}\left(1 + \frac{5}{2}\frac{\partial \ln N_d}{\partial \ln L}\right)$ and 2) $\frac{\partial \alpha_c}{\partial \tau_c} = \frac{\alpha_c(1-\alpha_c)}{\tau_c}$. Combining with equation (3) gives the resulting equation

$$RE_{aci} = -\overline{F^{\downarrow}}\phi_{atm}\frac{f_c\alpha_c(1-\alpha_c)}{3N_d}\left(1 + \frac{5}{2}\frac{\Delta \ln L}{\Delta \ln N_d} + \frac{3(\alpha_c - \alpha_{clr})}{\alpha_c(1-\alpha_c)}\frac{\Delta \ln f_c}{\Delta \ln N_d}\right)\overline{\Delta N_d} \tag{4}$$

which is used to compute the aerosol indirect shortwave radiative effect. The single-directional difference quotients, $\frac{\Delta \ln L}{\Delta \ln N_d}$ and $\frac{\Delta \ln f_c}{\Delta \ln N_d}$, are calculated using the slope of the linear least squares fit to variable combinations from each of the 4 aerosol experiments from over hourly intervals along the trajectory. The three terms inside the parentheses are regarded in order as the Twomey effect, liquid water path adjustment, and cloud fraction adjustment.

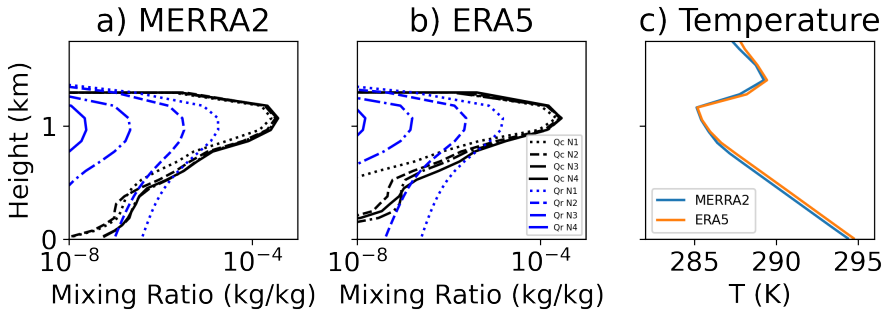

Figure S1. Vertical profile of the cloud water mixing ratio on 07/18/2017 averaged over an hour from 13:00 UTC simulated for pristine (N1; dotted), clean (N2; dashed), control (N3; dotted-dashed), and polluted (N4; solid) experiments using a) MERRA2 and b) ERA5 reanalysis meteorology for the boundary condition. Air temperature is from WRF using MERRA2 and ERA5 are displayed in (c).

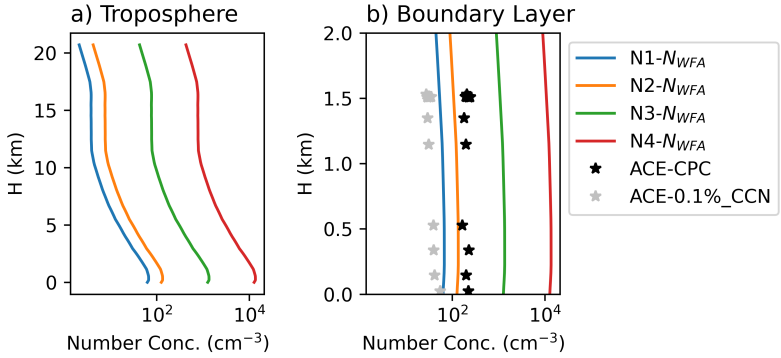

Figure S2. Vertical profile of the background number of water friendly aerosol (NWFA) concentrations for pristine (N1), clean (N2), control (N3), and polluted (N4) conditions on 7/18/17 at 13:00 UTC using the Thomspon (aerosol-aware) scheme plotted over the a) whole troposphere and b) boundary layer with observations of the total condensation particle counter (CPC; black asterisks) and CCN at 0.1% supersaturation (gray asterisks) from aircraft measurements taken between 10:00 – 16:00 UTC. Note, aerosol data is omitted in layers with cloud.

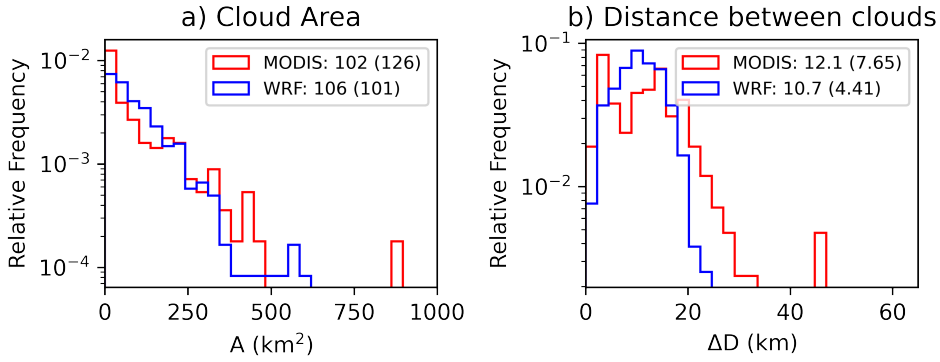

Figure S3. Histogram of the (a) areal extent and (b) minimum distance between cell centroids detected using the watershed algorithm for the 7/18/17 case study at 13:00 UTC. Means and standard deviation (shown in parenthesis) are shown for both MODIS (red) and WRF (blue) data sets.

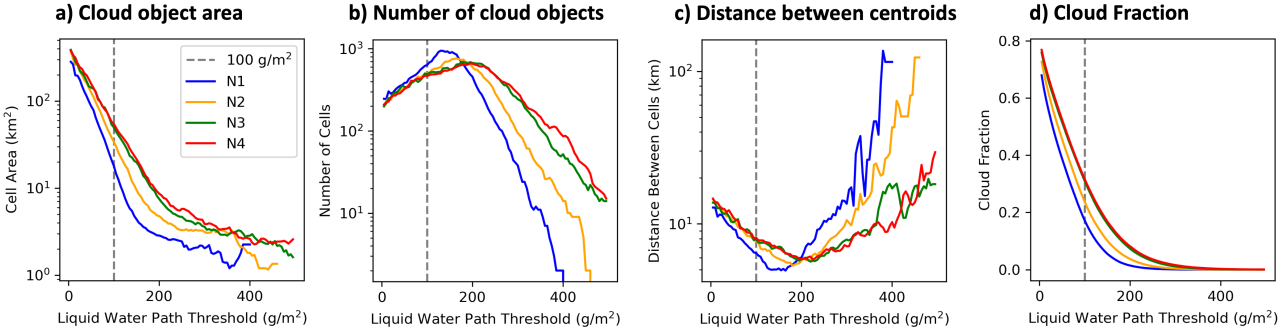

Figure S4. Cloud object area (a), number of clouds over the inner domain (b), and distance between clouds (c) as a function of the LWP threshold used to determine the cloud object boundries for pristine (blue), clean (orange), control (green), and polluted (red) WRF simulations. The dashed line represents the 100 g m^{-2} threshold used throughout the study.

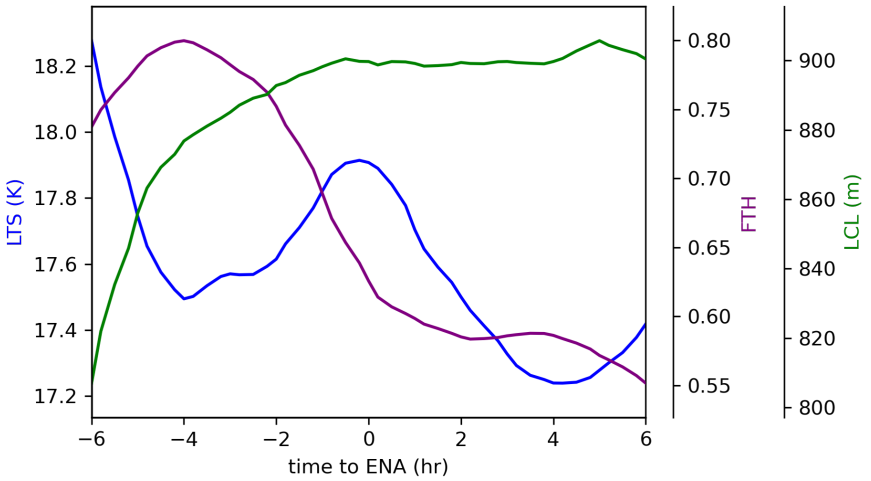

Figure S5. Lower tropospheric stability (i.e. the difference in potential temperature between the surface and 700 hPa; blue), free tropospheric humidity (relative humidity at 850 hPa; purple), and lifted condensation level (purple) computed using MERRA2 thermodynamic profiles along the 07/18/2017 trajectory case study.

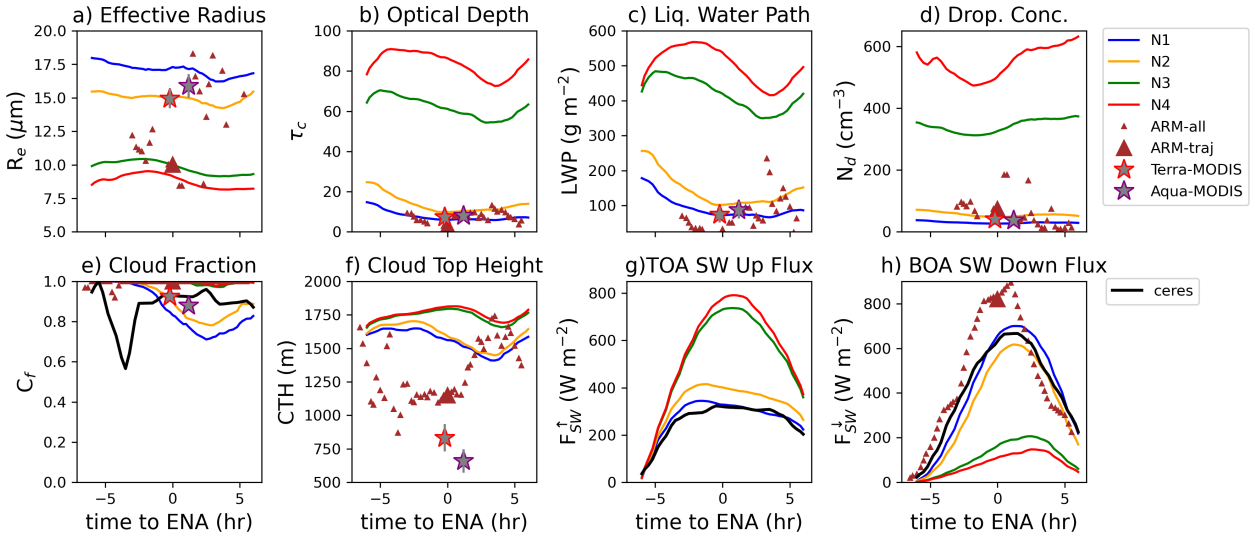

Figure S6. a) Droplet effective radius, b) cloud optical thickness, c) liquid water path, d) droplet concentration, e) liquid cloud fraction, f) cloud top height (CTH), g) top of atmosphere outgoing shortwave radiative flux ($F^{\uparrow}_{SW}$, and h) bottom of atmosphere incoming shortwave flux ($F^{\downarrow}_{SW}$ for pristine (blue), clean (orange), control (green), and polluted (red) WRF simulations. WRF-Solar was used for comparison with the satellite retrievals. ARM (brown diamond) retrievals are provided at all time steps and at the time when the trajectory passes over the ARM site (larger brown diamond) and MODIS retrievals from satellites Terra (red star) and Aqua (blue star) are provided when available along the trajectory on 07/15/2017. Note, aside from time to ENA equals 0, the ARM measurements do not coincide with the trajectory location and are merely used to show Eulerian variability.

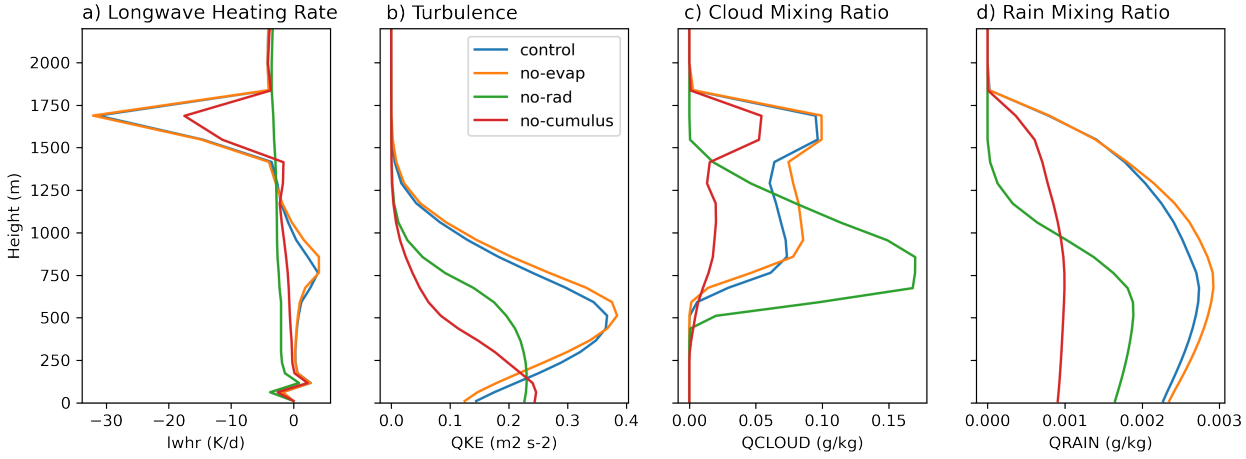

Figure S7. Vertical profile of the a) longwave radiative cooling rate, b) turbulent kinetic energy, c) cloud water mixing ratio, and d) rain water mixing ratio for the control, no evaporative cooling from cloud and rain drops, no radiation to cloud layer, and turning off the cumulus scheme from the WRF experiments for the case study day 07/15/2017 at 13:00 UTC.

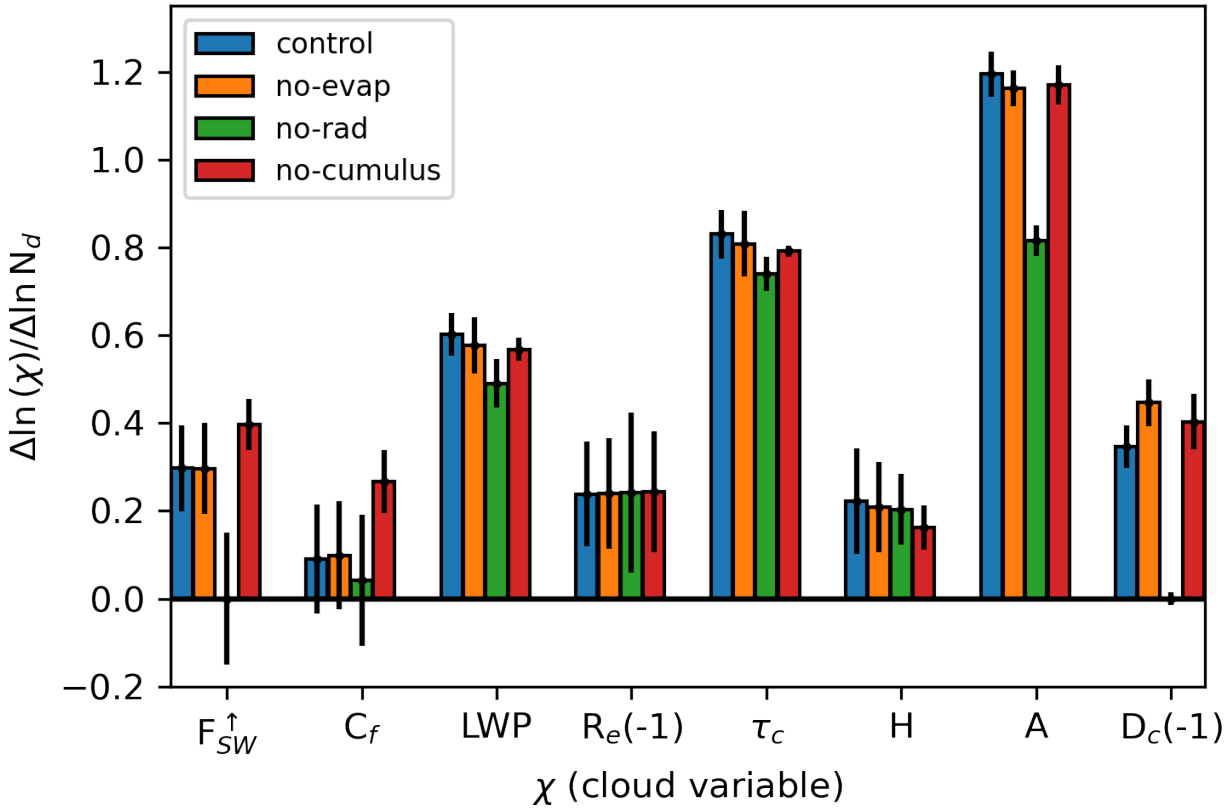

Figure S8. Value of the slope in the log change of a given variable (χ) to the log change in cloud droplet number concentration (N_d) computed from 2 aerosol WRF experiments simulations on for the control, no evaporative cooling from cloud and rain drops, no radiation to cloud layer, and turning off the cumulus scheme from the WRF experiments for the case study day 07/15/2017 at 13:00. χ variables shown are: top of atmosphere outgoing shortwave flux ($F^{\uparrow}_{SW}$), liquid cloud fraction (C_f), liquid water path (LWP), effective droplet radius (R_e), cloud optial thickness (τ_c), and cloud thickness (H)

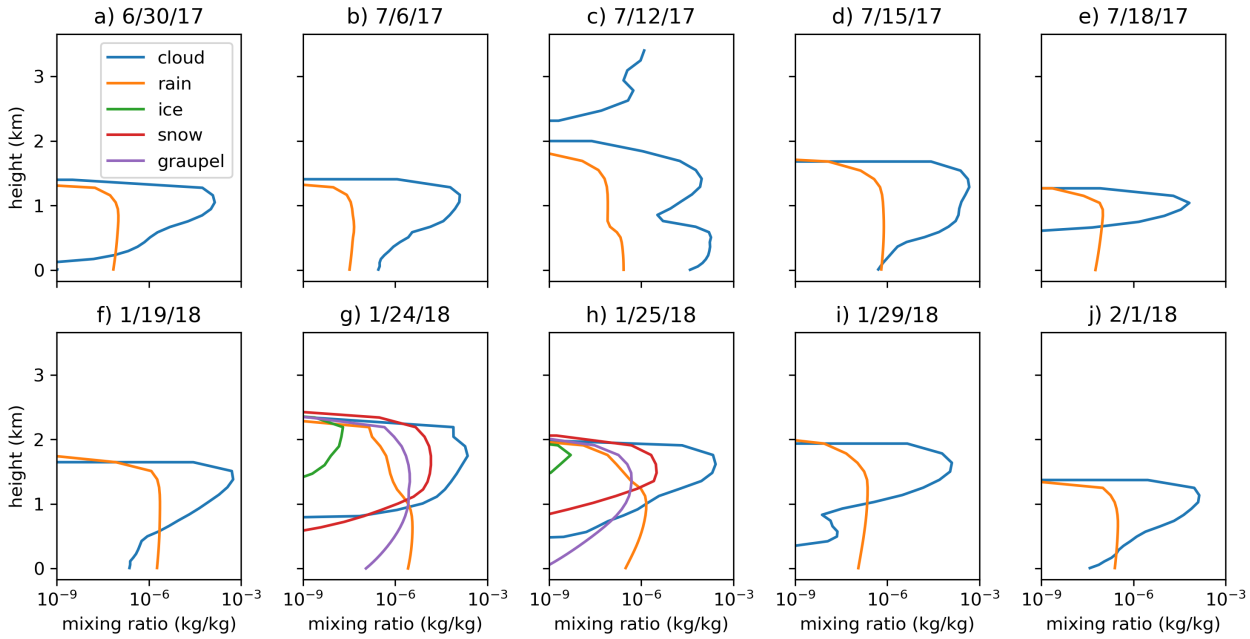

Figure S9. Vertical profile of the cloud, rain, ice, snow, and graupel mixing ratios for each case study at 13:00 UTC simulated for the control aerosol experiment using MERRA-2 reanalysis metoerology for the boundary condition.

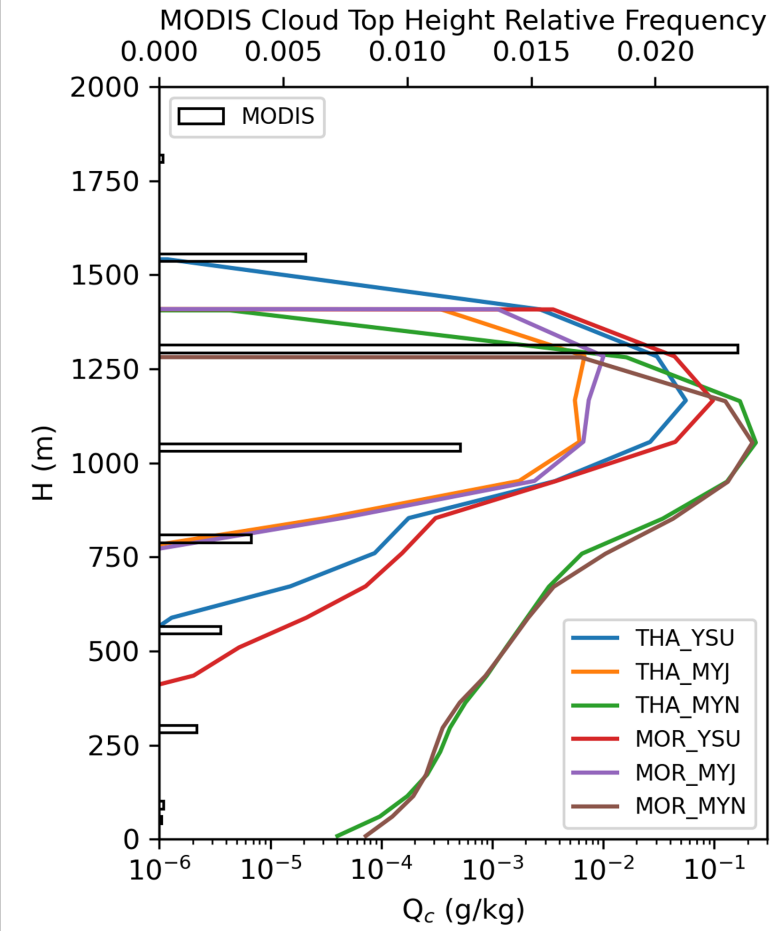

Figure S10. Vertical profile of cloud water mixing ratio (Q_c) from each of the microphysics and PBL scheme combinations described in Table 2. Normalized histogram of MODIS cloud top height retrievals (black rectangles) are plotted on a separate x-axis.

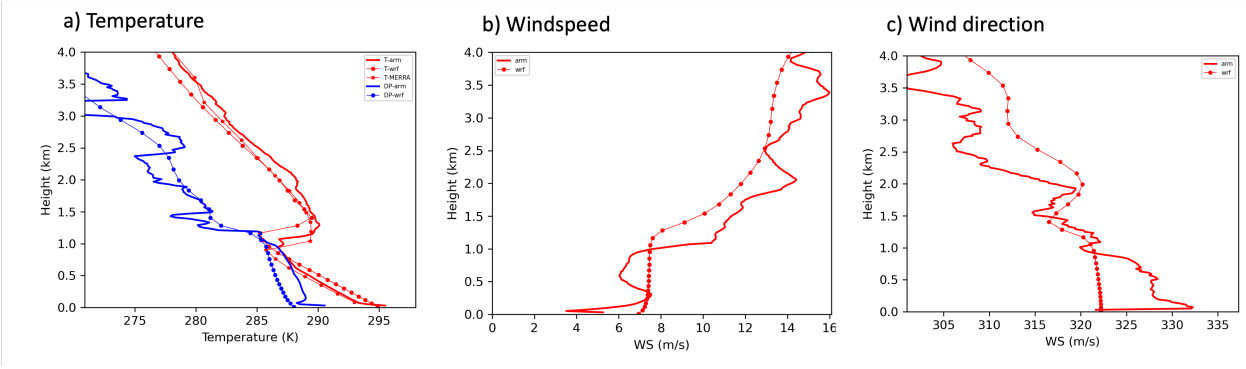

Figure S11. a) Vertical profile of air temperature (red) and dewpoint temperature (blue) from interpsonde measurements at the arm site at Graciosa Island (solid), as well as the simulations from WRF (solid with circles) and raw MERRA2 data, b) wind speed, and c) wind direction from ARM measurements and WRF simulations on 7/18/2017 at 13:00 UTC.

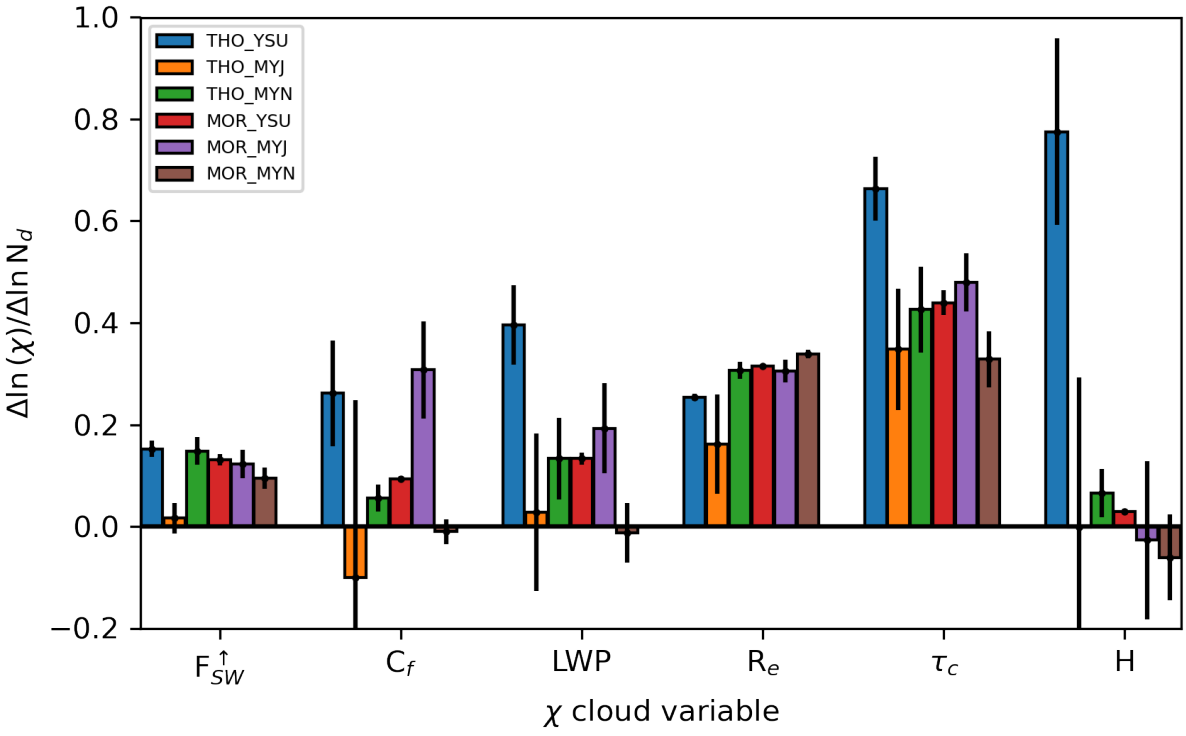

Figure S12. Value of the slope in the log change of a given variable (χ) to the log change in cloud droplet number concentration (N_d) computed from 4 aerosol WRF experiments simulations on 7/18 represented at 13:00 UTC for 6 different WRF configurations; 3 PBL schemes (YSU, MYJ, MYN) and 2 microphysics schemes (Thompson and Morrison). χ variables shown are: top of atmosphere outgoing shortwave flux ($F^{\uparrow}_{SW}$), liquid cloud fraction (C_f), liquid water path (LWP), effective droplet radius (R_e), cloud optial thickness (τ_c), and cloud thickness (H)

References

Christensen, M. W., Gettelman, A., Cermak, J., Dagan, G., Diamond, M., Douglas, A., Feingold, G., Glassmeier, F., Goren, T., Grosvenor, D. P., Gryspeerdt, E., Kahn, R., Li, Z., Ma, P.-L., Malavelle, F., McCoy, I. L., McCoy, D. T., McFarquhar, G., Mülmenstädt, J., Pal, S., Possner, A., Povey, A., Quaas, J., Rosenfeld, D., Schmidt, A., Schrödner, R., Sorooshian, A., Stier, P., Toll, V., Watson-Parris, D., Wood, R., Yang, M., and Yuan, T.: Opportunistic experiments to constrain aerosol effective radiative forcing, Atmospheric Chemistry and Physics, 22, 641–674, https://doi.org/10.5194/acp-22-641-2022, 2022.

Christensen, M. W., Ma, P.-L., Wu, P., Varble, A. C., Mülmenstädt, J., and Fast, J. D.: Evaluation of aerosol–cloud interactions in E3SM using a Lagrangian framework, Atmospheric Chemistry and Physics, 23, 2789–2812, https://doi.org/10.5194/acp-23-2789-2023, 2023.

Diamond, M. S., Director, H. M., Eastman, R., Possner, A., and Wood, R.: Substantial Cloud Brightening From Shipping in Subtropical Low Clouds, AGU Advances, 1, e2019AV000 111, https://doi.org/10.1029/2019AV000111, 2020.

Grosvenor, D. P., Sourdeval, O., Zuidema, P., Ackerman, A., Alexandrov, M. D., Bennartz, R., Boers, R., Cairns, B., Chiu, J. C., Christensen, M., Deneke, H., Diamond, M., Feingold, G., Fridlind, A., Hunerbein, A., Knist, C., Kollias, P., Marshak, A., McCoy, D., Merk, D., Painemal, D., Rausch, J., Rosenfeld, D., Russchenberg, H., Seifert, P., Sinclair, K., Stier, P., van Diedenhoven, B., Wendisch, M., Werner, F., Wood, R., Zhang, Z., and Quaas, J.: Remote Sensing of Droplet Number Concentration in Warm Clouds: A Review of the Current State of Knowledge and Perspectives, Reviews of Geophysics, 56, 409–453, https://doi.org/10.1029/2017RG000593, 2018.

Hersbach, H., Bell, B., Berrisford, P., Hirahara, S., Horányi, A., Muñoz-Sabater, J., Nicolas, J., Peubey, C., Radu, R., Schepers, D., Simmons, A., Soci, C., Abdalla, S., Abellan, X., Balsamo, G., Bechtold, P., Biavati, G., Bidlot, J., Bonavita, M., De Chiara, G., Dahlgren, P., Dee, D., Diamantakis, M., Dragani, R., Flemming, J., Forbes, R., Fuentes, M., Geer, A., Haimberger, L., Healy, S., Hogan, R. J., Hólm, E., Janisková, M., Keeley, S., Laloyaux, P., Lopez, P., Lupu, C., Radnoti, G., de Rosnay, P., Rozum, I., Vamborg, F., Villaume, S., and Thépaut, J.-N.: The ERA5 global reanalysis, Quarterly Journal of the Royal Meteorological Society, 146, 1999–2049, https://doi.org/https://doi.org/10.1002/qj.3803, 2020.

Quaas, J., Boucher, O., Bellouin, N., and Kinne, S.: Satellite-based estimate of the direct and indirect aerosol climate forcing, Journal of Geophysical Research: Atmospheres, 113, https://doi.org/10.1029/2007JD008962, 2008a.

Quaas, J., Boucher, O., Bellouin, N., and Kinne, S.: Satellite-Based Estimate of the Direct and Indirect Aerosol Climate Forcing, Journal of Geophysical Research: Atmospheres, 113, D05 204, https://doi.org/10.1029/2007jd008962, 2008b.

Stephens, G. L.: Radiation profiles in extended water clouds. II: Parameterization schemes, Journal of the Atmospheric Sciences, 35, 2123–2132, 1978.